Enhanced power conversion efficiency of quantum dot sensitized solar cells with near single-crystalline TiO$_2$ nanohelixes used as photoanodes

Seung Hee Lee,[1] Ho Jin,[2] Dong-Yeong Kim,[1] Kyung Song,[1] Sang Ho Oh,[1] Sungjee Kim,[2] E. Fred Schubert,[3] and Jong Kyu Kim[1,*]

[1]*Department of Materials Science and Engineering, Pohang University of Science and Technology (POSTECH), 77 Cheongam-Ro, Nam-Gu, Pohang, Gyeongbuk, 790-784, South Korea*
[2]*Department of Chemistry, Pohang University of Science and Technology (POSTECH), 77 Cheongam-Ro, Nam-Gu, Pohang, Gyeongbuk, 790-784, South Korea*
[3]*Department for Electrical, Computer, and Systems Engineering, Rensselaer Polytechnic Institute, 110 Eighth Street, Troy, New York 12180, USA*
[*]*kimjk@postech.ac.kr*

Abstract: Photo-electrodes with tailored three-dimensional nanostructures offer a large enhancement in light harvesting capability for various optoelectronic devices enabled by strong light scattering in the nanostructures as well as improved charge transport. Here we present an array of three-dimensional titanium dioxide (TiO$_2$) nanohelixes fabricated by the oblique angle deposition method as a multifunctional photoanode for CdSe quantum dot sensitized solar cells (QDSSCs). The CdSe QDSSC with a TiO$_2$ nanohelix photoanode shows a 100% higher power conversion efficiency despite less light being absorbed in CdSe QDs when compared with a conventional TiO$_2$ nanoparticle photoanode. We attribute the higher power conversion efficiency to strong light scattering by the TiO$_2$ nanohelixes and much enhanced transport and collection of photo-generated carriers enabled by the unique geometry and near-single crystallinity of the TiO$_2$ nanohelix structure.

©2014 Optical Society of America

OCIS codes: (230.0230) Optical devices; (230.0250) Optoelectronics.

References and links

1. B. O'Regan and M. Grätzel, "A low-cost, high-efficiency solar cell based on dye-sensitized colloidal TiO$_2$ films," Nature **353**(6346), 737–740 (1991).
2. N. Tétreault and M. Grätzel, "Novel nanostructures for next generation dye-sensitized solar cells," Energy Environ. Sci. **5**(9), 8506–8516 (2012).
3. A. Hagfeldt, G. Boschloo, L. Sun, L. Kloo, and H. Pettersson, "Dye-sensitized solar cells," Chem. Rev. **110**(11), 6595–6663 (2010).
4. M. Grätzel, "Solar energy conversion by dye-sensitized photovoltaic cells," Inorg. Chem. **44**(20), 6841–6851 (2005).
5. F. Pichot, J. Pitts, and B. Gregg, "Low-temperature sintering of TiO$_2$ colloids: Application to flexible dye-sensitized solar cells," Langmuir **16**(13), 5626–5630 (2000).
6. A. P. Alivisatos, "Semiconductor clusters, nanocrystals, and quantum dots," Science **271**(5251), 933–937 (1996).
7. W. W. Yu, L. H. Qu, W. Z. Guo, and X. G. Peng, "Experimental determination of the extinction coefficient of CdTe, CdSe, and CdS nanocrystals," Chem. Mater. **15**(14), 2854–2860 (2003).
8. L. Brus, "Electronic wave functions in semiconductor clusters: Experiment and theory," J. Phys. Chem. **90**(12), 2555–2560 (1986).
9. Q. Shen, A. Yamada, S. Tamura, and T. Toyoda, "CdSe quantum dot-sensitized solar cell employing TiO$_2$ nanotube working-electrode and Cu$_2$S counter-electrode," Appl. Phys. Lett. **97**(12), 123107 (2010).
10. A. J. Nozik, "Quantum dot solar cells," Physica E **14**(1–2), 115–120 (2002).

11. M. C. Hanna and A. J. Nozik, "Solar conversion efficiency of photovoltaic and photoelectrolysis cells with carrier multiplication absorbers," J. Appl. Phys. **100**(7), 074510 (2006).
12. P. V. Kamat, "Quantum dot solar cells. Semiconductor nanocrystals as light harvesters," J. Phys. Chem. C **112**(48), 18737–18753 (2008).
13. V. González-Pedro, X. Xu, I. Mora-Seró, and J. Bisquert, "Modeling high-efficiency quantum dot sensitized solar cells," ACS Nano **4**(10), 5783–5790 (2010).
14. J.-W. Lee, D.-Y. Son, T. K. Ahn, H.-W. Shin, I. Y. Kim, S.-J. Hwang, M. J. Ko, S. Sul, H. Han, and N.-G. Park, "Quantum-dot-sensitized solar cell with unprecedentedly high photocurrent," Sci. Rep. **3**, 1050–1057 (2013).
15. P. K. Santra and P. V. Kamat, "Mn-doped quantum dot sensitized solar cells: A strategy to boost efficiency over 5%," J. Am. Chem. Soc. **134**(5), 2508–2511 (2012).
16. Q. Zhang and G. Cao, "Nanostructured photoelectrodes for dye-sensitized solar cells," Nano Today **6**(1), 91–109 (2011).
17. Q. Zhang, D. Myers, J. Lan, S. A. Jenekhe, and G. Cao, "Applications of light scattering in dye-sensitized solar cells," Phys. Chem. Chem. Phys. **14**(43), 14982–14998 (2012).
18. K. D. Benkstein, N. Kopidakis, J. van de Lagemaat, and A. J. Frank, "Influence of the percolation network geometry on electron transport in dye-sensitized titanium dioxide solar cells," J. Phys. Chem. B **107**(31), 7759–7767 (2003).
19. K. Zhu, T. B. Vinzant, N. R. Neale, and A. J. Frank, "Removing structural disorder from oriented TiO_2 nanotube arrays: Reducing the dimensionality of transport and recombination in dye-sensitized solar cells," Nano Lett. **7**(12), 3739–3746 (2007).
20. S. H. Kang, S. H. Choi, M. S. Kang, J. Y. Kim, H. S. Kim, T. Hyeon, and Y. E. Sung, "Nanorod-based dye-sensitized solar cells with improved charge collection efficiency," Adv. Mater. **20**(1), 54–58 (2008).
21. J. Nelson, "Continuous-time random-walk model of electron transport in nanocrystalline TiO_2 electrodes," Phys. Rev. B **59**(23), 15374–15380 (1999).
22. J. van de Lagemaat, N.-G. Park, and A. J. Frank, "Influence of electrical potential distribution, charge transport, and recombination on the photopotential and photocurrent conversion efficiency of dye-sensitized nanocrystallne TiO_2 solar cells: A study by electrical impedance and optical modulation techniques," J. Phys. Chem. B **104**(9), 2044–2052 (2000).
23. M. Law, L. E. Greene, J. C. Johnson, R. Saykally, and P. Yang, "Nanowire dye-sensitized solar cells," Nat. Mater. **4**(6), 455–459 (2005).
24. X. Feng, K. Zhu, A. J. Frank, C. A. Grimes, and T. E. Mallouk, "Rapid charge transport in dye-sensitized solar cells made from vertically aligned single-crystal rutile TiO_2 nanowires," Angew. Chem. **124**(11), 2781–2784 (2012).
25. X. Feng, K. Shankar, O. K. Varghese, M. Paulose, T. J. Latempa, and C. A. Grimes, "Vertically aligned single crystal TiO_2 nanowire arrays grown directly on transparent conducting oxide coated glass: Synthesis details and applications," Nano Lett. **8**(11), 3781–3786 (2008).
26. J. B. Baxter and E. S. Aydil, "Nanowire-based dye-sensitized solar cells," Appl. Phys. Lett. **86**(5), 053114 (2005).
27. J. Zhou, B. Song, G. Zhao, W. Dong, and G. Han, "TiO_2 nanorod arrays sensitized with CdS quantum dots for solar cell applications: Effects of rod geometry on photoelectrochemical performance," Appl. Phys., A Mater. Sci. Process. **107**(2), 321–331 (2012).
28. B. Liu and E. S. Aydil, "Growth of oriented single-crystalline rutile TiO_2 nanorods on transparent conducting substrates for dye-sensitized solar cells," J. Am. Chem. Soc. **131**(11), 3985–3990 (2009).
29. E. Galoppini, J. Rochford, H. Chen, G. Saraf, Y. Lu, A. Hagfeldt, and G. Boschloo, "Fast electron transport in metal organic vapor deposition grown dye-sensitized ZnO nanorod solar cells," J. Phys. Chem. B **110**(33), 16159–16161 (2006).
30. M. Wang, J. Bai, F. Le Formal, S.-J. Moon, L. Cevey-Ha, R. Humphry-Baker, C. Grätzel, S. M. Zakeeruddin, and M. Grätzel, "Solid-state dye-sensitized solar cells using ordered TiO_2 nanorods on transparent conductive oxide as photoanodes," J. Phys. Chem. C **116**(5), 3266–3273 (2012).
31. K. Zhu, N. R. Neale, A. Miedaner, and A. J. Frank, "Enhanced charge-collection efficiencies and light scattering in dye-sensitized solar cells using oriented TiO_2 nanotubes arrays," Nano Lett. **7**(1), 69–74 (2007).
32. G. K. Mor, K. Shankar, M. Paulose, O. K. Varghese, and C. A. Grimes, "Use of highly-ordered TiO_2 nanotube arrays in dye-sensitized solar cells," Nano Lett. **6**(2), 215–218 (2006).
33. are S. Lee, I. J. Park, D. H. Kim, W. M. Seong, D. W. Kim, G. S. Han, J. Y. Kim, H. S. Jung, and K. S. Hong, "Crystallographically preferred oriented TiO_2 nanotube arrays for efficient photovoltaic energy conversion," Energy Environ. Sci. **5**(7), 7989–7995 (2012).
34. A. B. F. Martinson, J. W. Elam, J. T. Hupp, and M. J. Pellin, "ZnO nanotube based dye-sensitized solar cells," Nano Lett. **7**(8), 2183–2187 (2007).
35. R. Mohammadpour, A. Iraji Zad, A. Hagfeldt, and G. Boschloo, "Comparison of trap-state distribution and carrier transport in nanotubular and nanoparticulate TiO_2 electrodes for dye-sensitized solar cells," ChemPhysChem **11**(10), 2140–2145 (2010).
36. M. Adachi, Y. Murata, J. Takao, J. Jiu, M. Sakamoto, and F. Wang, "Highly efficient dye-sensitized solar cells with a titania thin-film electrode composed of a network structure of single-crystal-like TiO_2 nanowires made by the "oriented attachment" mechanism," J. Am. Chem. Soc. **126**(45), 14943–14949 (2004).

37. Y. Q. Wang, Y. M. Sun, and K. Li, "Dye-sensitized solar cells based on oriented ZnO nanowire-covered TiO$_2$ nanoparticle composite film electrodes," Mater. Lett. **63**(12), 1102–1104 (2009).
38. C. H. Ku and J. J. Wu, "Electron transport properties in ZnO nanowire array/nanoparticle composite dye-sensitized solar cells," Appl. Phys. Lett. **91**(9), 093117 (2007).
39. S. Yodyingyong, Q. F. Zhang, K. Park, C. S. Dandeneau, X. Y. Zhou, D. Triampo, and G. Z. Cao, "ZnO nanoparticles and nanowire array hybrid photoanodes for dye-sensitized solar cells," Appl. Phys. Lett. **96**(7), 073115 (2010).
40. W. Peng, M. Yanagida, L. Han, and S. Ahmed, "Controlled fabrication of TiO2 rutile nanorod/anatase nanoparticle composite photoanodes for dye-sensitized solar cell application," Nanotechnology **22**(27), 275709 (2011).
41. Q. Zheng, H. Kang, J. Yun, J. Lee, J. H. Park, and S. Baik, "Hierarchical construction of self-standing anodized titania nanotube arrays and nanoparticles for efficient and cost-effective front-illuminated dye-sensitized solar cells," ACS Nano **5**(6), 5088–5093 (2011).
42. J. Nayak, K. Prabakar, J. W. Park, and H. Kim, "Effect of synthesis temperature on structure, optical and photovoltaic properties of TiO$_2$ nanorod thin films," Electrochim. Acta **65**, 44–49 (2012).
43. J. van de Lagemaat and A. J. Frank, "Nonthermalized electron transport in dye-sensitized nanocrystalline TiO$_2$ films: Transient photocurrent and random-walk modeling studies," J. Phys. Chem. B **105**(45), 11194–11205 (2001).
44. N.-G. Park, J. van de Lagemaat, and A. J. Frank, "Effect of morphology on electron transport in dye-sensitized nanostructured TiO$_2$ films," J. Photosci. **10**, 199–205 (2003).
45. Z.-S. Wang, H. Kawauchi, T. Kashima, and H. Arakawa, "Significant influence of TiO$_2$ photoelectrode morphology on the energy conversion efficiency of N719 dye-sensitized solar cell," Coord. Chem. Rev. **248**(13–14), 1381–1389 (2004).
46. P. Sudhagar, J. H. Jung, S. Park, Y. G. Lee, R. Sathyamoorthy, Y. S. Kang, and H. Ahn, "The performance of coupled (CdS:CdSe) quantum dot-sensitized TiO$_2$ nanofibrous solar cells," Electrochem. Commun. **11**(11), 2220–2224 (2009).
47. M. M. Hawkeye and M. J. Brett, "Glancing angle deposition: Fabrication, properties, and applications of micro- and nanostructured thin films," J. Vac. Sci. Technol. A **25**(5), 1317–1335 (2007).
48. K. Robbie and M. J. Brett, "Sculptured thin films and glancing angle deposition: Growth mechanics and applications," J. Vac. Sci. Technol. A **15**(3), 1460–1465 (1997).
49. K. D. Harris, A. Huizinga, and M. J. Brett, "High-speed porous thin film humidity sensors," Electrochem. Solid State Lett. **5**(11), H27–H29 (2002).
50. G. K. Kiema and M. J. Brett, "Effect of thermal annealing on structural properties and electrochemical performance of carbon films with porous microstructures," J. Electrochem. Soc. **151**(5), E194–E198 (2004).
51. B. Djurfors, J. N. Broughton, M. J. Brett, and D. G. Ivey, "Microstructural characterization of porous manganese thin films for electrochemical supercapacitor applications," J. Mater. Sci. **38**(24), 4817–4830 (2003).
52. S. R. Kennedy, M. J. Brett, H. Miguez, O. Toader, and S. John, "Optical properties of a three-dimensioal silicon square spiral photonic crystal," Cryst. Photonics Nanostruct. **1**(1), 37–42 (2003).
53. A. L. Elias, K. D. Harris, C. W. M. Bastiaansen, D. J. Broer, and M. J. Brett, "Large-area microfabircation of three-dimensional, helical polymer structures," J. Micromech. Microeng. **15**(1), 49–54 (2005).
54. H. Jin, S. Choi, R. Velu, S. Kim, and H. J. Lee, "Preparation of multilayered CdSe quantum dot sensitizers by electrostatic layer-by-layer assembly and a series of post-treatments toward efficient quantum dot-sensitized mesoporous TiO$_2$ solar cells," Langmuir **28**(12), 5417–5426 (2012).
55. W. W. Yu, Y. A. Wang, and X. Peng, "Formation and stability of size-, shape-, and structure-controlled CdTe nanocrystals: Ligand effects on monomers and nanocrystals," Chem. Mater. **15**(22), 4300–4308 (2003).

1. Introduction

Dye sensitized solar cells (DSSCs) have received tremendous attention due to their much reduced manufacturing costs, capability for achieving a high power conversion efficiency (PCE), and relative ease of fabrication [1–5]. One of the factors limiting the performance of DSSCs is the lack of available dyes with an extended long-wavelength absorption edge, which motivates the use of quantum dots (QDs); such QDs have a high extinction coefficient, a tunable peak absorption energy that can be adjusted by controlling the QD size, and the capability for multiple exciton generation [6–11]. As a consequence, QD-sensitized solar cells (QDSSCs) are attracting great interest for highly promising next-generation photovoltaic devices [12–15].

Solar cells generate electricity through two sequential steps; first, the generation of charge carrier pairs via light absorption and, second, the transport and collection of the carriers. Especially in (Q)DSSCs, the photoanode plays a crucial role in both sequential steps, thereby strongly affecting the PCE. The geometry of a photoanode determines the degree of light scattering and absorption, and thus, the light harvesting efficiency, while the crystallinity of a

photoanode affects the electrical conductivity, and thus, the transport of photo-generated charge carriers. Thin films made of sintered TiO_2 nanoparticles (~20nm diameter) are widely used as photoanodes for (Q)DSSCs due to their large surface area that is amenable for the adsorption of dye molecules and QDs [16]. However, there are two significant drawbacks of these conventional sintered TiO_2 photoanodes. First, the scattering of incident light which generally increases the probability of photon-QDs interaction, is negligible because the size of the TiO_2 nanoparticles is much smaller than the wavelength range of the absorbed solar irradiation [17]. Thus, additional scattering layers consisting of *big* TiO_2 nanoparticles whose diameter is comparable to the wavelength of sun light, are incorporated on top of the film consisting of sintered *small* nanoparticles. Second, the transport of carriers through entangled complex networks of sintered nanoparticles is poor due to long percolated carrier travel lengths for charge collection [18,19], and numerous grain boundaries between sintered nanoparticles that promote recombination and very slow trap-limited diffusion of carriers [19–22].

Various one-dimensional nanostructures such as nanowire [23–26], nanorod [20,27–30] and nanotube [31–34] have been demonstrated as photoanodes for improving the transport of electrons by providing direct conduction pathways with reduced trapping and recombination at the grain boundaries [35]. Although these one-dimensional nanostructures showed improved carrier transport properties, the smaller surface area of nanoparticle electrodes caused less absorption of QDs/dye molecules, i.e. less light harvesting [36]. This drawback has been partly overcome by the hybridization of nanoparticles and one-dimensional nanostructures [37–41], however, such hybrid photoanodes still suffer from very limited light scattering and little enhancement in transport properties; thus a lower-than-expected PCE has been attained.

In this study, we present a new multifunctional photoanode based on an array of three-dimensional TiO_2 nanohelixes for strongly enhanced electron transport properties as well as stronger light scattering, and consequently for a remarkably increased PCE of Cadmium Selenide (CdSe) QDSSCs. Structural properties of three-dimensional TiO_2 nanohelixes fabricated by oblique angle deposition are investigated by scanning electron microscopy (SEM), X-ray diffraction (XRD) and transmission electron microscopy (TEM). Optical and electrical properties of the photoanodes are systematically investigated by simulations and experiments. CdSe QDSSCs based on the TiO_2 nanohelix array showed 100% higher PCE over those with the conventional nanoparticle photoanode despite lower amount of absorbed CdSe QDs.

2. Results and discussion

2.1 Fabrication of QDSSCs with TiO₂ nanohelix array

Figure 1(a) shows a schematic description of the QDSSC investigated here. It consists of a photoanode based on an array of TiO_2 nanohelixes sensitized with QDs on a FTO coated glass substrate, a CuS-coated FTO counter electrode, and infiltrated electrolyte between the electrodes. Figure 1(b) shows a cross-sectional SEM image of an array of ~5μm-thick TiO_2 nanohelixes grown vertically on the substrate. As shown in the SEM top view image in the inset, the TiO_2 nanohelix array provides space sufficiently open for the penetration of QDs and the redox electrolyte.
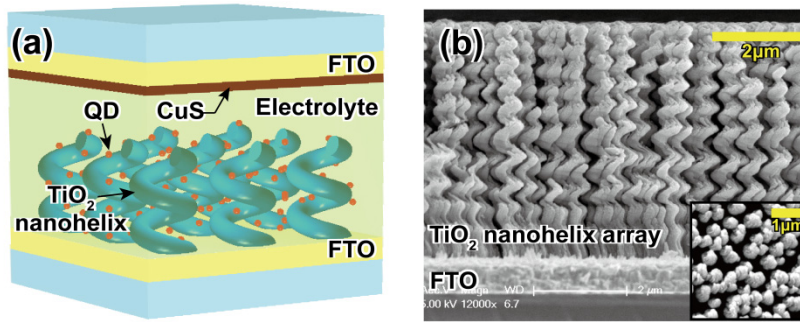
Fig. 1. (a) Schematic diagram of a QD-sensitized solar cell based on TiO$_2$ nanohelix array. SEM images of the (b) cross-sectional and (inset) top view of the fabricated TiO$_2$ nanohelixes array on a FTO-coated glass substrate showing a very porous structure facilitating the penetration of QDs and electrolyte into the pores.

2.2 Structural properties of TiO$_2$ nanohelix array

The micro-structure of the TiO$_2$ nanohelixes strongly affects the transport and collection of photo-generated charge carriers. The micro-structural evolution of the TiO$_2$ nanohelixes upon thermal annealing was investigated by XRD, as shown in Fig. 2. The XRD peaks from the as-deposited sample are all identified as those of the FTO substrate; there was no single peak assignable to TiO$_2$-related phases. New diffraction peaks appeared after thermal annealing at 500°C for 30minutes and they can be indexed as the anatase phase of TiO$_2$. The XRD results indicate that the as-deposited amorphous phase TiO$_2$ nanohelixes were transformed to the anatase phase during thermal annealing.
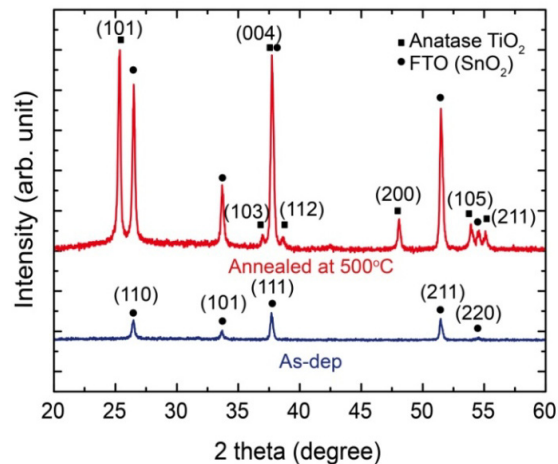

Fig. 2. X-ray diffraction patterns of an as-deposited (blue trace) and an annealed (red trace) TiO$_2$ nanohelix array on a FTO glass substrate.

The microstructure and crystallinity of the annealed TiO$_2$ nanohelixes were characterized by using TEM. Figures 3(a) and 3(b) show a bright-field TEM image of a bundle of TiO$_2$ nanohelixes and corresponding diffraction pattern, respectively. The spot diffraction pattern as well as pronounced diffraction contrast of the TEM image indicates the high crystallinity of anatase TiO$_2$ nanohelixes. Dark-field TEM images formed with separate diffraction spots [c, d, and e indicated by yellow circles in Fig. 3(b)] allows us to estimate the size of grains constituting the nanohelixes [Figs. 3(c) and 3(e)] since a similar intensity contrast region in a dark field image indicates that the orientations of the lattice planes are similar to the selected

diffraction spot. Note that each nanohelix is composed of large TiO_2 grains with the average size of $413 \pm 25nm$ along the growth direction, which corresponds to ~1.5 times the pitch of a helix [the pitch of nanohelix is marked in Fig. 3(a)]. The high-resolution TEM (HRTEM) image taken from one of the grains shows near-single crystalline lattice fringes which are indexed as the lattice planes of the anatase phase of TiO_2 [Fig. 3(f)]. TiO_2 nanohelixes consisting of such large grains with high crystallinity can act as "express way" for the transport of photo-generated electrons; in other words, the photo-generated electrons can be efficiently transported through the nanohelixes with a much lower probability of recombination at grain boundaries when compared with a sintered TiO_2 nanoparticle network that typically have a much smaller grain size.
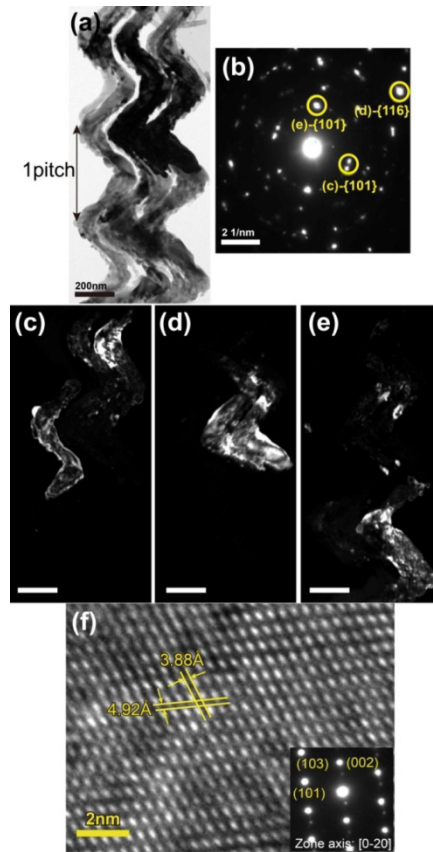

Fig. 3. (a) Bright-field TEM image of a bundle of TiO_2 nanohelixes. (b) Selected diffraction pattern taken from a region in (a). (c)-(e) Dark-field TEM images formed by selecting the diffraction spots indicated in (b): (c) {101}; (d) {116}; and (e) {101} reflections of TiO_2 anatase phase. Scale bars in TEM images: 200 nm. (f) HRTEM image and electron diffraction pattern (inset) taken from one of the grains in an annealed TiO_2 nanohelix. Note that (002) plane appears due to double diffraction.

The CdSe QDs loaded TiO_2 nanohelixes were indeed confirmed in the high-angle annular dark-field (HAADF) mode of scanning TEM [Fig. 4(a)]. The HAADF imaging mode is useful to distinguish CdSe from TiO_2 since the difference in average atomic numbers of CdSe and TiO_2 causes a difference in HAADF intensities. In the HAADF shown in Fig. 4a, CdSe QDs are clearly distinguishable from the TiO_2 nanohelix, showing that the QDs are densely packed and dispersed rather uniformly over the helix surface. The energy dispersive X-ray spectrum (EDS) obtained from one of the bright spots [see inset in Fig. 4(a)] further confirmed the presence of the elements Cd and Se. Note that Ti and O are detected as well

since the electron probe transmits electrons also into the TiO_2, through the CdSe QDs, thereby generating X-rays from both crystals. Figure 4b shows a HRTEM image of a QD-loaded TiO_2 nanohelix. The lattice fringes of both CdSe and TiO_2 are clearly resolved. In addition, Moiré fringes are frequently observed due to the overlap of the two lattices (CdSe and TiO_2), indicating that both crystals have the excellent crystallinity. Based on the microstructural analyses by XRD and TEM, the TiO_2 nanohelixes consisting of large grains with uniformly covered by densely packed CdSe QDs are expected to enhance the generation and transport of photo-generated carriers.
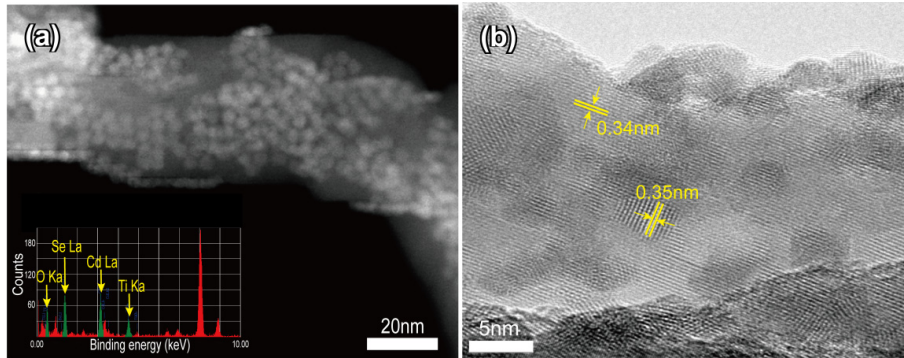

Fig. 4. (a) Low magnification STEM HAADF image of a TiO_2 nanohelix loaded with CdSe QDs (bright spots). Different average atomic numbers of CdSe and TiO_2 cause different HAADF intensities. The presence of CdSe QDs on TiO_2 was further confirmed by an EDS measurement as shown in the inset. (b) HRTEM image of the CdSe QDs that are loaded on a TiO_2 nanohelix. The measured lattice spacings of TiO_2 (0.34 nm) and CdSe (0.35 nm) are indicated.

2.3 Optical properties of TiO2 nanohelix array

Absorbance values of a CdSe QDs-loaded TiO_2 nanohelix array and a TiO_2 nanoparticle reference layer with same thickness on FTO/glass substrates were measured as a function of wavelength, as shown in Fig. 5. The absorbance of the nanohelix array is much higher than that of the nanoparticle over the entire visible wavelength range. There are two representative factors determining the absorbance of photoanodes – the amount of loaded QDs and the light scattering effect. In order to figure out which factor makes major contribution to the higher absorbance in the nanohelix array, we estimated the surface area of both photoanodes considering the geometrical features observed by SEM and the porosities estimated by ellipsometry. The estimated surface area in $3 \times 3 \times 3 \mu m^3$ volume of the nanoparticle layer is $6.0 \times 10^{-9} m^2$, ~22 times larger than that of the nanohelixes layer ($2.7 \times 10^{-10} m^2$) Since, the amount of the loaded QDs is generally proportional to the surface area of the structures [42], thus, it can be regarded that the nanoparticle layer contains much larger amount of loaded QDs than the nanohelix array. Despite less QDs loading, the nanohelix array shows much higher absorbance even outside of the QDs absorption band, which is attributed to strong light scattering effect caused by the three-dimensional TiO_2 nanohelix array.
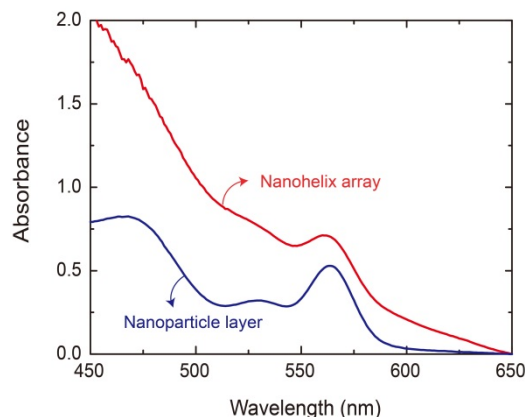
Fig. 5. Absorbance of CdSe QDs loaded on a TiO$_2$ nanohelix array layer (red) and TiO$_2$ nanoparticle layer (blue) on FTO/glass substrates.

The effect of light scattering in various photoanode structures was simulated using the commercial finite element method software COMSOL Multiphysics. Figures 6(a)–6(d) show different geometries of the modelled structures (such as a stack of TiO$_2$ nanoparticles, a TiO$_2$ nanorod, a TiO$_2$ nanotube, and a TiO$_2$ nanohelix) and the corresponding electric field distribution at the surfaces and surroundings of each structure when an x-polarized electromagnetic wave is incident in normal direction from the FTO substrate side. Perfect electric conductors (PEC) condition was imposed on two boundary surfaces perpendicular to x-axis, and perfect magnetic conductors (PMC) condition was applied to two boundary surfaces perpendicular to y-axis for considering the periodicity of the structures. [Note that the scale for the stacked nanoparticles in Fig. 6(a) is smaller than for the other structures due to much smaller size of the nanoparticles (~20nm).] The incident electromagnetic wave (with wavelength of 550nm) passing through the stack of nanoparticles, the nanorod, and the nanotube seems to be guided along the structures maintaining its periodicity. However, much more complex distribution of electric field with ~3 times higher amplitude than other structures is observed in both the surrounding region and the surface area of the nanohelix, which is attributed to the strong light scattering effect of the three-dimensional nanohelix structure. On the other hand, the electromagnetic wave propagates through the stack of nanoparticles with negligible light scattering because the size of nanoparticles is much smaller than the wavelength of incident light [17]. Meanwhile, one-dimensional nanorods and nanotubes having comparable sizes (diameters) to the incident wavelength have a lower ability to scatter the incident light than the three-dimensional nanohelix. The probability for propagating photons to encounter an interface between the TiO$_2$ nanostructures and air, in other words, the light scattering cross-section, is much greater for the three-dimensional nanostructure array than for the one-dimensional nanostructure arrays.
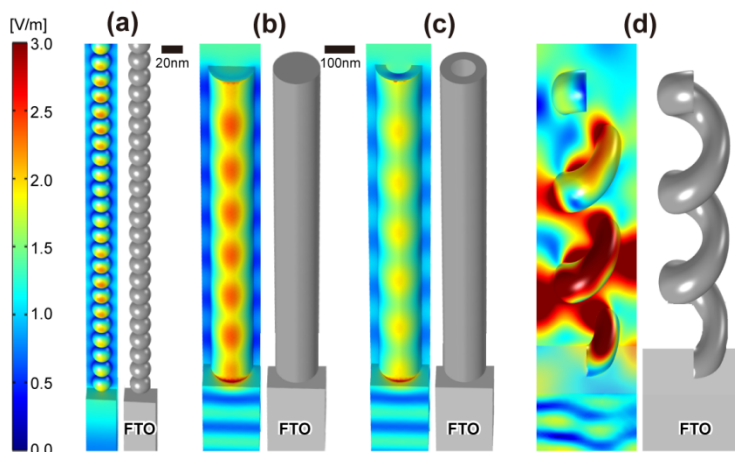
Fig. 6. The geometry (right) and the simulated electric field distribution (left) at the surface of (a) stacked TiO$_2$ nanoparticles (10nm radius, 30nm period), (b) a TiO$_2$ nanorod (75nm radius, 200nm period), (c) a TiO$_2$ nanotube (70nm inner, 75nm outer radius, 200nm period), and (d) a TiO$_2$ nanohelix (125nm helix radius, 75nm wire radius, 600nm period) on the FTO substrates when x-polarized electromagnetic wave is incident. The periodic boundary condition is imposed along in-plane direction of the FTO in each simulation. Identical scale bar (shown on left side) for the electric field strength is applied to (b), (c) and (d).

In order to experimentally verify the enhanced light scattering by the three-dimensional TiO$_2$ nanohelix array, the diffuse transmittance of the 5μm-thick TiO$_2$ nanohelix array layer and the 5μm-thick TiO$_2$ nanoparticle layer on FTO glass and bare FTO glass were measured. Inset of Fig. 7(a) shows a schematic diagram of specular and diffused optical transmission. The total transmittance through the samples was measured by using an integrated sphere, so that both diffusely and specularly transmitted light were collected, whereas the specular transmittance was measured without an integrated sphere.

In results, the bare FTO substrate sample shows the highest total transmittance and specular transmittance among the three samples as shown in Fig. 7(a). With a 5 μm-thick TiO$_2$ nanoparticle layer on top of the FTO substrate sample, both the total transmittance and the specular transmittance decrease by a similar ratio and tendency with respect to the wavelength of incident light. In case of the TiO$_2$ nanohelixes array/FTO sample, both transmittances are much lower than for the other two samples. Then, the diffuse transmittance was estimated by subtracting the specular transmittance from the total transmittances of each sample. Figure 7(b) shows the diffuse transmittance curves together with the absorption curve of the CdSe QD sensitizer (shown by the yellow shaded region) as a function of wavelength. Diffuse transmittance through the TiO$_2$ nanohelix array layer is higher than the TiO$_2$ nanoparticle layer and bare FTO glass over the entire visible wavelength region, indicating a much stronger light scattering effect – i.e. much more spreading of incident light – by the TiO$_2$ nanohelixes. Note that the diffuse transmittance through the nanohelix array layer is 4.3 times higher than through the TiO$_2$ nanoparticle layer near the band edge of the CdSe QD sensitizer. The diffuse transmittance of the nanoparticle layer is slightly higher than that of the FTO glass, indicating that light scattering by the nanoparticles exists, but the amount is negligible. A photograph made of the three samples located on a string of red characters ("POSTECH") is shown in the inset of Fig. 7(b). Enhanced light scattering by the nanohelix array obstructs the visibility of characters while the characters are clearly visible through the nanoparticle sample and the bare FTO glass. Interestingly, the diffuse transmittance of the nanoparticle layer and bare FTO glass sample decreases exponentially with the wavelength of the incident light, whereas that of the nanohelix array shows a quite different trend, which, we

believe, is attributed to different light scattering mechanisms involved, i.e. Rayleigh scattering for the nanoparticle sample and Mie scattering for the nanohelix array sample. The nanostructure size enabling Mie scattering is approximately half of the incident light's wavelength while Rayleigh scattering occurs for nanostructures even if their feature size is much smaller size than the wavelength [17]. Therefore, the origin of the wavelength-dependent diffuse transmittance through the nanoparticle layer and bare substrate is presumed to be Rayleigh scattering in which scattering cross section is inversely proportional to the 4th power of the wavelength. On the other hand, in case of nanohelix array, Mie scattering presumably is predominant. Such enhanced light scattering by the three-dimensional photoanode nanostructures increases the travelling length of light in the active layer which increases the probability of photons to interact with the sensitizers; this desirable effect can compensate for the lower light absorption ability caused by relatively smaller surface area of the nanohelix photoanode when compared to conventional nanoparticle-based photoanode.
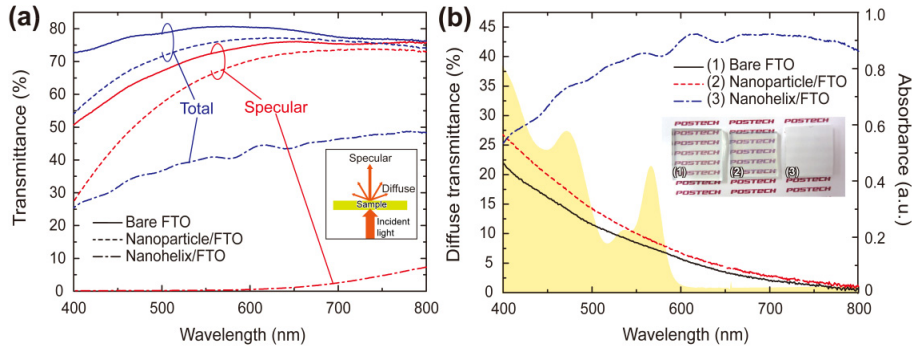

Fig. 7. (a) Measured total and specular transmittances of a bare FTO/glass substrate, the 5 μm-thick TiO$_2$ nanoparticle layer, and 5 μm-thick TiO$_2$ nanohelix array layer on a FTO/glass substrate as a function of the wavelength of the incident light. Inset: Schematic diagram of specular and diffuse optical transmission when monochromatic light is normally incident at the bottom of the FTO/glass substrate. (b) Diffuse transmittances of bare FTO coated glass (black solid line), nanoparticle layer film (red dotted line) and nanohelix array film (blue dotted-dashed line) on the FTO coated glass obtained by measuring the total transmittance and specular transmittance as function of wavelength from 400 to 800nm. Photographs of each sample (see inset) clearly show the difference in the amount of light scattering. The spectrum filled in yellow indicates the absorbance of the synthesized CdSe QD solution (right axis). The peak near at 560nm is attributed to absorption by CdSe QDs.

2.4 Photovoltaic performance

The photocurrent-density-versus-voltage (*J-V*) characteristics of CdSe QDSSCs based on a 5μm-thick TiO$_2$ nanohelix array and 5μm-thick TiO$_2$ nanoparticles reference were measured under simulated AM1.5 (100mW/cm^2) solar illumination, as shown in Fig. 8(a). The photovoltaic parameters calculated from the J-V characteristics are summarized in Table 1. The 5μm nanohelix array based QDSSC shows a 1.6 times higher short-circuit current density (*J$_{sc}$*) (5.74mA/cm^2) than nanoparticle layer based cell (3.60mA/cm^2) with same thickness. Although the nanohelixes have much less surface area for the adsorption of QDs than the nanoparticles, the former induce a strong light scattering effect by their unique three-dimensional geometry enabling much higher light harvesting and short-circuit photocurrent density. The open circuit voltage (*V$_{oc}$*) of the QDSSC with nanohelix array (0.49V) compares favourably to the *V$_{oc}$* of the QDSSC with nanoparticle layer (0.40V) because the former has a high diffusion coefficient and thus low charge-carrier recombination.

Electron transport properties of each photoanode were evaluated by measuring the electron transport time by means of intensity modulated photocurrent spectroscopy with a 530nm illuminating light source using a wide range of light intensities, ranging from 5 to

100W/m^2. The electron transport time in the 3.4μm nanohelix layer based photoanode is one order of magnitude faster than in the 10.8μm nanoparticle layer based photoanode. In order to consider the different thicknesses of the photoanodes for a fair evaluation of charge transport characteristics, the electron diffusion coefficient (D_n) was calculated using the equation: $D_n = d^2/4\tau_c$ where d is the thickness of the film in which electrons travel and τ_c is electron transport time [43,44]. Fig. 8(b) shows the electron transport time and diffusion coefficient of the QDSSCs as function of incident 530nm laser light intensity. The results demonstrate that the promotion of electron transport in the near-single crystalline TiO$_2$ nanohelix makes electron transport time shorter due to a four times higher diffusion coefficient when compared with a conventional nanoparticle layer. In addition, the openly structured film composed of nanohelixes makes mass transport resistance small [45], in other words, a better penetration of the electrolyte into the porous nanohelix array favourably affects the V_{oc} to yield a high V_{oc} [46]. The low surface area of nanohelixes makes the probability of unwanted re-combination between photo-generated electron charges and electrolyte or QDs low and also results in a strongly enhanced V_{oc}. Consequently, in spite of the smaller amount of adsorbed QDs (due to the smaller specific surface area for the nanohelix photoanode), the CdSe QDSSC based on the TiO$_2$ nanohelix array shows a two-fold improvement in overall solar energy conversion efficiency (1.34%) over the QDSSC based on the nanoparticle layer (0.66%). Although the PCE values of our QDSSC are somewhat lower than that of recent state-of-the-art QDSSCs with newly developed QDs for wide absorption range, electrolytes, and appropriate post-treatments, we believe that our concept can make further improvement in the PCE of such high-performance QDSSCs.
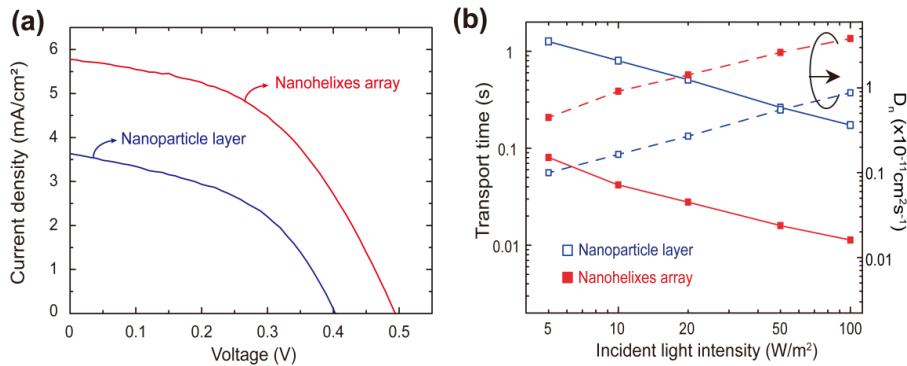

Fig. 8. (a) J-V characteristics of QDSSCs based on a TiO$_2$ nanoparticle photoanode and a TiO$_2$ nanohelix photoanode both having 5μm thickness under the condition of simulated AM 1.5 solar radiation with 100mW/cm^2 intensity. (b) Measured electron transport times (left axis) of nanoparticle and nanohelix array based QDSSCs by intensity modulated photocurrent spectroscopy (IMPS) as a function of incident light intensity using a 530nm laser. Diffusion coefficients (D_n, right axis) are calculated from the electron transport times and thickness of each photoanode.

Table 1. Comparison of Photovoltaic Parameters of QDSSCs Calculated from the *J-V* Curves in Fig. 8.

Sample	J_{sc} [mA/cm^2]	V_{oc} [V]	FF	Efficiency [%]
Nanohelix	5.74	0.49	0.48	1.34
Nanoparticle	3.60	0.40	0.25	0.66

3. Experimental section

3.1 Preparation of TiO₂ photoanodes

In order to fabricate the TiO_2 nanohelix array, a cleaned fluorine-doped SnO_2 (FTO) glass substrate was masked to define the active region ($2 \times 5mm^2$); then the TiO_2 nanohelix array was formed by oblique angle deposition [47, 48] using an electron beam evaporator. Oblique angle deposition is a very attractive method that is able to fabricate a variety of nanostructures due to its great versatility, position/shape-controllability, reproducibility, and compatibility with conventional micro-electronics processes. In oblique angle deposition, the substrate is tilted with respect to the incident vapor flux unlike typical physical vapor deposition methods. At the initial stage of the deposition, nuclei form on the substrate, producing self-shadowed regions with respect to the obliquely incident vapor flux. Subsequent vapor flux cannot deposit in the self-shadowed regions, but preferentially deposits on the high point (tip) of the nuclei, thereby creating an array of slanged nanorods. In addition, by rotating the substrate during the oblique deposition, various three-dimensional nanostructures (such as nanohelixes and nano zig-zags), can be fabricated. Although oblique angle deposition by electron-beam evaporation for fabricating three-dimensional nanohelixes array may be more costly than typical doctor-blade method used for nanoparticles coating, its advantages and performance enhancements enabled by various three-dimensional nanostructures would eliminate the potential cost trade-off. In addition, e-beam evaporation is a well-matured technique compatible with current microelectronics technology, which enables uniform, high-quality deposition of any evaporable materials by a batch process, thus, the capability of large area deposition on multiple wafer (or cell) scale can be achieved by appropriate chamber size and design. Various applications utilizing the advantages of the oblique angle deposition have been demonstrated [49–53]. For fabricating a TiO_2 nanohelix array, the substrate was tilted against vapor flux at 80°, and repeated rotation with a speed of 1rpm for 2 seconds followed by a pause for 12 seconds; the film deposition rate was 5Å/s. Then, the as-deposited TiO_2 nanohelix array on the FTO glass substrate was annealed at 500°C for 30 minutes under air ambient. The reference sample has a 5µm-thick TiO_2 nanoparticle layer that was formed by doctor blade-printing with a commercial TiO_2 paste (Ti-Nanoxide, T20/SP: average nano-particle size of about 20nm).

3.2 Fabrication and measurements of QDSSCs

For fabricating QDSSCs based on TiO_2 nanohelix arrays and nanoparticle layer photoanodes, TiO_2 nanohelix arrays and doctor-bladed nanoparticles on FTO glass substrate were dipped into a prepared CdSe QD solution for 12 hours, so that the QDs adsorbed on the TiO_2 helixes by the electrostatic attractive force between negatively charged CdSe QDs and positively charged TiO_2 [54]. CdSe QDs were used as sensitizer due to its matching conduction band edge alignment with TiO2, and excellent photo- and chemical stability in polymide electrolytes. The loading of the CdSe QDs on the TiO_2 nanohelix surface was investigated by a scanning TEM equipped with an energy dispersive spectrometer. After QDs loading, the working electrode was assembled into a sandwich type cell using a CuS on a FTO glass counter electrode [55]. The cell was sealed by a hot-pressing process using a 50µm thick polymer sheet (Himilan of Mitsui-DuPont poly chemical). Finally, polysulfide electrolyte solution with 1.0M Na_2S and 1.0M S in water was injected into the solar cell's gap between two electrodes through a pre-drilled hole, and the hole was sealed by hot pressing. For solar cell performance characterization, the cell was irradiated by $100mW/cm^2$ of light from a 300W xenon lamp of a solar simulator (model 66902, Newport). The electron transport properties were measured by intensity modulated photocurrent spectroscopy (IMPS).

4. Conclusion

In summary, we have demonstrated a three-dimensional TiO_2 nanohelix array, fabricated by the oblique angle deposition method, as a multifunctional photoanode for high performance quantum dot (CdSe) sensitized solar cells (QDSSCs). The TiO_2 nanohelix array based QDSSCs showed much improved photovoltaic characteristics with a V_{oc} of 0.49V, a J_{sc} of 5.74mA/cm^2, and consequently two times higher PCE than conventional nanoparticle based QDSSCs having same thickness. The enhanced performance of nanohelix array based QDSSC is attributed to two important sequential improvements; first, a boost in the number of photo-generated carriers due to strong light scattering and, second, a very efficient collection of photo-generated carriers through near-single crystalline nanohelix structures. The array of aligned nanohelixes consisting of reduced number of inter-crystallite grain boundaries allows for injected photo-generated carriers to be rapidly transported due to a high diffusion coefficient in the photoanode (four times higher than conventional nanoparticle layer based photoanode). In addition, the three-dimensional nanohelix structure effectively scatters incident light, so that the interaction of light with QD sensitizers increases, resulting in strongly enhanced light harvesting which in turn results in a high J_{sc}. Therefore, more photons are absorbed by the QDs and more carriers survive the unwanted charge recombination, which leads to the improved PCE of the QDSSC. These favorable results inspire the use of three-dimensional metal oxide nanostructures to extend their application in optoelectronic devices particularly photoelectrochemical cells and organic photovoltaics.